Chapter 14
Wavelet Methods in Computational Combustion

Robert Prosser and R. Stewart Cant

Abstract Discretisation schemes based on the use of wavelet methods offer many potential advantages for the numerical simulation of combustion. In many cases of interest, flame structures are thin relative to the largest length scales of the problem and most length scales of the flow field, and so lend themselves to simulation using adaptive-mesh methods. Wavelet methods are naturally adaptive, in that the coefficients of the wavelet transform are non-zero only in regions where there is significant variation present in the solution. Hence, simple thresholding can be employed to make valuable savings in storage and in execution time. In this chapter, the basic principles of wavelet methods are established. Orthogonal and biorthogonal wavelet formulations are described and their advantages and disadvantages are discussed. An illustration of a wavelet-based discretisation scheme is provided using the Navier-Stokes momentum equation as an example. The same wavelet approach is applied to the simulation of a one-dimensional laminar premixed flame for which an asymptotic solution exists. Comparisons are made between the computational and analytical results and the accuracy of the wavelet approach is assessed. Extensions to higher dimensions are discussed. Finally, the current state of development of wavelet methods is outlined and conclusions are drawn.

14.1 Introduction

High-fidelity numerical simulation of turbulent combustion is a very demanding task. Techniques such as Direct Numerical Simulation (DNS) and Large Eddy Simulation (LES) require the flow field to be represented in three spatial dimensions

Robert Prosser
School of MACE, University of Manchester, Manchester M60 1QD, UK, e-mail: robert.prosser@manchester.ac.uk

R. Stewart Cant
Cambridge University, Cambridge, CB2 1PZ, UK, e-mail: rsc10@eng.cam.ac.uk

T. Echekki, E. Mastorakos (eds.), *Turbulent Combustion Modeling*,
Fluid Mechanics and Its Applications 95, DOI 10.1007/978-94-007-0412-1_14,

and cannot make use of statistical symmetries of the problem in the same manner as the traditional Reynolds-Averaged Navier Stokes (RANS) approach. Moreover, the flow field is evolving in time, and hence it is essential to use time-accurate solution methods in order to capture the flow, the flame and the full complexity of their interactions. All of this is computationally expensive, especially when the requirement is for full spatial and temporal resolution of all relevant phenomena, as is the case in DNS.

In turbulent flow, the computational expense follows directly from the range of length and time scales that must be represented. In combustion problems, it is most often the case that there are further length and time scales even shorter than those of the turbulent flow field. The very smallest scales are associated with the diffusion-reaction layers deep within the flame structure, and these tend to be highly localised in space, at least on an instantaneous basis. Here the computational expense arises mainly from the tendency of the flame structure to move around within the domain due to the effects of advection by the flow field and propagation due to heat conduction and molecular diffusion. This means that sufficient computational mesh support must be provided to ensure proper spatial resolution everywhere in the domain. The time-advancement algorithm must be applied at every spatial mesh point, and hence the computational cost is set.

There have been many attempts to exploit the localised nature of the flame structure using adaptive mesh refinement (AMR) techniques [9, 28]. Here, the computational mesh is refined locally in order to provide high resolution only in regions of the domain (such as within the flame) where there are steep spatial gradients. Conversely, the mesh can be made less dense in regions where there is little activity in the solution. Since the flame structure typically occupies only a small part of the total volume of the domain, considerable computational cost savings can be made without a net loss of resolution. Considerable progress has been made and the utility of the approach has been demonstrated. Nevertheless it is difficult to apply such techniques while retaining high-order accuracy, and there are major issues concerning their efficient implementation on massively-parallel computers.

Ideally, an adaptive spectral method is required which would allow for very high spatial accuracy coupled with a capability for dynamic local mesh refinement. Methods based on Fourier transforms have been used for many years in simulations of turbulence, offering excellent accuracy but lacking the flexibility and spatial localisation necessary for use in an adaptive manner. More recently, wavelet transforms have emerged as a possible framework in which to build a class of numerical methods offering high accuracy combined with solution adaption. Wavelets, unlike the more familiar Fourier basis functions, are localised in both the spatial and spectral domains, and have many other interesting properties which make them an attractive prospect for use in future combustion simulations.

This article introduces wavelet analysis in the context of combustion DNS, outlines the relevant mathematical background and describes the application of wavelet techniques within a suitable numerical solution method. Results are presented which indicate the power of the approach, and conclusions are drawn.

14.2 Wavelet Transforms

14.2.1 Orthogonal Wavelets

A wavelet transform can be interpreted in much the same way as a Fourier transform. Where the two differ is in the choice of the basis function employed. In the Fourier setting, the basis is chosen to be the complex exponential. In the wavelet transform, there are actually two basis functions: the *scaling function* and the *wavelet*. The scaling function can be interpreted as a low resolution band pass filter, while the wavelet represents the complementary high resolution band pass filter [21].

The wavelet decomposition is based on the repeated application of a two-scale relationship. In particular, we have [8]

$$\begin{aligned} \bigoplus_{i=-\infty}^{\infty} \mathbf{W}_i &= L^2(\mathbb{R}) \\ \mathbf{V}_J &= \mathbf{V}_{J-1} \oplus \mathbf{W}_{J-1} \\ \mathbf{V}_i &\perp \mathbf{W}_i \end{aligned} \tag{14.1}$$

where $\bigoplus$ represents the *direct sum*. Equation 14.1(a) indicates that $L^2(\mathbb{R})$ can decomposed into a family of *wavelet spaces* $\mathbf{W}_i$. Each wavelet space forms half of a partnership with a *scaling function space* $\mathbf{V}_i$. i characterizes the resolution of the spaces with $i \to \infty$ as the resolution is refined. The basis for the scaling function space is denoted $\phi_{i,k}(x) \equiv \phi\left(2^i x - k\right)$, and the basis for the wavelet space is $\psi_{i,k} \equiv \psi\left(2^i x - k\right)$. Factors of $\sqrt{2}$ can appear in these definitions, depending on the choice of normalization. On the real line, both the wavelet and scaling function exhibit scale and translation invariance.

The projection of $f(x) \in L^2(\mathbb{R})$ is accomplished by taking the inner product with respect to the basis, i.e.

$$f(x) = \sum_{i=-\infty}^{\infty} Q_i(f)(x),$$

where Q_i is the projector onto $\mathbf{W}_i$ which, in the case of *orthogonal* basis functions can be written as

$$Q_i(f)(x) = \sum_{k\in\mathbb{Z}} < f(u), \psi_{i,k}(u) > \psi_{i,k}(x). \tag{14.2}$$

The two scale relation defined by Eq. 14.1 allows the wavelet projection to be written in terms of scaling function projections;

$$Q_i(f)(x) = (P_{i+1}(f) - P_i(f))(x)$$

where

$$P_i(f)(x) = \sum_{k\in\mathbb{Z}} < f(u), \phi_{i,k}(u) > \phi_{i,k}(x). \tag{14.3}$$

Equation 14.1(b) provides the basis for the practical implementation of a wavelet decomposition for finite domains. Assume for simplicity that we have a finite dimensional representation of some periodic function $f(x) \in [0,1)$, which is sampled on 2^J grid points $x_{J,k} = k2^{-J}$, $0 \leq k < 2^J$. If $f(x)$ is approximated by $P_J(f)(x)$ then an application of the two scale relation allows us to write

$$P_J(f) = (P_{J-1} + Q_{J-1})(f)(x). \tag{14.4}$$

The orthogonality of $\mathbf{V}_i$ and $\mathbf{W}_i$ implies that the two projectors P_{J-1} and Q_{J-1} lead to complementary representations of $P_J(f)$ on reduced dimensional spaces (in this case, each representation is defined on grids of resolution 2^{J-1}). In the first pass of the transform then, a vector of length 2^J is replaced with 2 vectors of length 2^{J-1}, but the key observation here is that the wavelet projection $Q_{J-1}(f)$ is *sparse*, by which we mean that many of the 2^{J-1} coefficients arising from the wavelet projection are close to zero. The defining property of the wavelet transform is that the resulting coefficients are only non-trivial when the analyzing wavelets are close to regions of rapid change. Such a feature makes wavelets a natural tool with which to explore flame structures, wherein two relatively static regions (reactants and products, or fuel and oxidiser) are separated by a region of rapid change (the flame). The sparsity of the wavelet representation is exploited via *thresholding*, in which those wavelet coefficients with a magnitude less than a user specified threshold ε are discarded with a minimal loss of accuracy (in a sense that can be made precise, i.e. see [12]). Hence, the two scale representation with thresholding allows us to replace a vector of dimension 2^J, with one comprising $O\left(2^{J-1}\right)$ components—$P_{J-1}(f)$ contains 2^{J-1} non-zero components, and Q_{J-1} typically contains a much reduced number of 'large' wavelet coefficients. The actual number of retained coefficients depends on the smoothness of the analyzed function $f(x)$.

Equation 14.4 can be repeatedly applied to $P_{J-1}(f)$ to obtain

$$\begin{aligned} P_J(f)(x) &= (P_{J-2} + Q_{J-2} + Q_{J-1})(f)(x) \\ &\vdots \\ &= P_0(f)(x) + \sum_{i=0}^{J-1} Q_i(f)(x) \end{aligned} \tag{14.5}$$

Equation 14.5 is the finite dimensional equivalent of Eq. 14.1(a). In practical calculations involving wavelets on the interval, the lower limit appearing in the sum of Eq. 14.5 is larger than zero. This reflects the need to keep the support of the wavelets smaller than the discretized interval. One final point to note is that the mapping $f(x) \to P_J(f)(x)$ requires an initial projection quadrature. This quadrature is usually approximate—many authors choose instead to use the sample values of the initial discretisation as the set of scaling function coefficients.

The implementation of the wavelet transform can take a number of forms. For some basis functions, the transform can be accomplished by a modified FFT [23]. In the most common approach (which makes use of Daubechies compact wavelet

[8]), the transform takes the form of a repeated finite difference-like operation (once for each space on each resolution). The weights associated with these operations are the *quadrature mirror filter coefficients* defining the wavelet. Examples of the implementation of wavelet transforms can be found in e.g. [24].

14.2.2 Biorthogonal Wavelet Transforms

Much of the utility of the wavelet transform emerges from the unique properties of the chosen wavelet, but there are also a number of problems with the orthogonal representations described in the previous section. In the orthogonal setting, many different choices of wavelet exist, some of which are more suitable for CFD applications than others. From a purely practical point of view many choices of wavelets do not have compact support (i.e. [23])—this implies that the inner products in Eqs. 14.2 and 14.3 effectively contain infinitely many quadrature filter coefficients and become difficult to evaluate. Such wavelets can be approximated as having compact support, but the resulting approximations lose their exact (to machine precision) orthogonality. Families of orthonormal wavelets with compact support do exist—the most famous examples being those of Daubechies [8]—but the orthogonal restraint leads to wavelets which are asymmetric.

For the simulation of fluid mechanics problems, asymmetric bases are undesirable as they introduce chirality into the numerical approximations for the governing equations [19, 20]. In addition the initial projection quadrature, which maps $f(x) \rightarrow P_J(f(x))$, is non-trivial and usually irreversible (to machine precision). In the setting of a collocation numerical scheme (or indeed any approach to the approximation of non-linear PDEs) the continual mapping to and from transformed representations leads to strong chirality and—eventually—instability in the numerical solution [25].

One approach to bypass the problems associated with chirality is to modify the wavelets by relaxing the constraint on orthogonality, to produce *biorthogonal* wavelet systems. Most of the relations described in the previous section hold for biorthogonal systems, but *two* sets of basis functions are required—the so-called *primal* and *dual* bases [6]. The scaling function and wavelet projectors are then written as

$$P_J(f) = \sum_{k \in Z} < f(u), \widetilde{\phi}_{J,k}(u) > \phi_{J,k}(x)$$
$$Q_J(f) = \sum_{k \in Z} < f(u), \widetilde{\psi}_{J,k}(u) > \psi_{J,k}(x),$$

where the tildes refer to the dual quantities. Biorthogonal wavelets contain sufficient flexibility to provide compact bases with symmetry—such considerations are particularly important in the construction of edge wavelets for bounded intervals [7]. The problem of the initial projection quadrature remains.

14.2.3 Second Generation Wavelets

A variant of the biorthogonal wavelet can be obtained via so-called *second generation wavelets*, pioneered by Sweldens and Donoho [12, 14, 27, 29, 30]. These wavelets are derived without recourse to Fourier transforms, and provide a simpler framework in which to define wavelets for more general settings than the real line. In addition, the classical biorthogonal wavelets of Cohen et al. [7] can be derived using the second generation approach. Finally, second generation wavelets circumvent the problems associated with an inexact initial projection quadrature.

There are two classes of wavelets proposed in the second generation framework: *interpolating wavelets* and *average interpolating wavelets* (i.e. see [27]) In this work, we choose the family of interpolating wavelets derived from the fundamental solutions discussed by Deslauriers and Dubuc [11]. In the second generation interpolating wavelet approach, the dual scaling function is defined by

$$\tilde{\phi}_{J,k} = \delta\left(x - k2^{-J}\right),$$

where $\delta(\cdot)$ is the Dirac delta function. The scaling functions and wavelets have compact support and are symmetric in the interior of a domain, in particular

$$\begin{aligned}\text{support}\left(\phi_{j,k}\right) &= \left[2^{-j}\left(m-(N-1)\right), 2^{-j}\left(m+(N-1)\right)\right],\\ \text{support}\left(\psi_{j,k}\right) &= [2^{-(j+1)}\left((2k+1)-(N-1)\right), 2^{-(j+1)}\left((2k+1)+(N-1)\right)].\end{aligned}$$

In this sense, we say that the coefficients $s_{j,k}$ and $d_{j,k}$ are respectively associated with the grid point $k2^{-1}$ and $(2k+1)2^{-(j+1)}$. Similar arguments can be made for the near boundary constructions, but the definitions become more algebraically complicated.

The dual scaling function (and indeed, the dual wavelet) are not members of $L^2(\mathbb{R})$, and the resulting transforms are limited in their range of application to smooth functions [12]. An alternative way of saying this is that the resultant wavelets do not strictly qualify as wavelets, since they do not satisfy the admissibility condition [8]

$$\int \psi(x)\,dx \neq 0.$$

The result of this inequality is that the wavelets are prone to aliasing, and do not conserve the integral of the original function:

$$\int P_i(f)\,dx \neq \int P_m(f)\,dx \quad i \neq m. \tag{14.6}$$

For classes of smooth function, this problem does not appear to be especially significant [12]; such conditions are typically encountered in the DNS of reacting flow wherein the smoothness of the resolved profiles—coupled with the limited number of allowable subspace decompositions—appears to minimize the effect of aliasing.

The projection of $f(x)$ onto the scaling function space leads to scaling function coefficients that are samples of the original function;

$$P_J(f)(x) = \sum_{k\in\mathbb{Z}} < f(u), \delta\left(u - k2^{-J}\right) > \phi_{J,k}(x)$$
$$= \sum_{k\in\mathbb{Z}} f\left(k2^{-J}\right)\phi_{J,k}(x) = \sum_{k\in\mathbb{Z}} f_{J,k}\phi_{J,k}(x).$$

It follows that $f_{J-1,k} = f_{J,2k}$ and hence successive scaling function approximations are subsamples of the original discretisation. The wavelet transform is given by

$$\begin{aligned} Q_i(f)(x) &= \sum_{k\in Z} d_{i,\alpha}\psi_{i,\alpha}(x) \\ &= (P_{i+1}(f) - P_i(f))(x) \\ &= \sum_{k\in\mathbb{Z}} f_{i+1,k}\phi_{i+1,k}(x) - \sum_{m\in\mathbb{Z}} f_{i,m}\phi_{i,m}(x) \\ d_{i,\alpha} &= Q_i(f)|_{x=(2\alpha+1)2^{-(i+1)}} \\ &= f_{i+1,2a+1} - \sum_{m\in\mathbb{Z}} \phi\left(\alpha + \frac{1}{2} - m\right) f_{i,m}. \end{aligned} \tag{14.7}$$

Clearly, the sparsity of the representation is governed by the properties of $\phi(\cdot)$. Furthermore, if the scaling function has compact support, it follows that $\phi(\alpha + 1/2 - m)$ comprises only finitely many non-zero entries, and Eq. 14.7 can be implemented as a finite difference-like operation.

14.3 Wavelets as a Method for DNS

We describe a collocation approach to the integration of the governing equations. The collocation strategy—where the wavelets are used merely to calculate derivatives [5]—provides a natural approach, since solution algorithms couched in terms of the transformed variables face formidable difficulties in evaluating the nonlinear terms associated with both convection and chemical reaction. For a 1-D flow domain Ω, we initially discretize the governing equations on to a regular mesh $G \subset \Omega$. As the solution evolves, we want to solve the equations only on those parts of the domain $G^\varepsilon \subset G$ where strong variations in the flow behaviour occur. Such behaviour might be found in, say, turbulent shear layers, or rapid temperature changes associated with chemical reaction. Wavelets are very good at picking up these regions of change, so a natural choice for the unstructured grid might be

$$G^\varepsilon = \{x_{i,\alpha} : |d_{i,\alpha}| > \varepsilon\}$$

where $d_{i,\alpha}$ is the wavelet coefficient associated with the point $x_{i,\alpha}$. If we try to calculate the derivatives on this mesh using traditional means, then we are left with the classical hanging node problem—those points at the outskirts of the unstructured mesh do not have sufficient neighbours to calculate their associated derivatives accurately. In the multiresolution approach however, we first calculate the wavelet ex-

pansion of the solution on G^{ε}. By construction, the coefficients on $G \backslash G^{\varepsilon}$ are small in magnitude (defined here as $|d_{i,\alpha}| < \varepsilon$) and may be omitted when calculating the approximate derivative. The resulting derivative can then be inverted on to the unstructured grid, and the solution time advanced as normal. The difficulty in this approach lies now in calculating the wavelet transform on the unstructured mesh. Methods for achieving this are available (i.e. [26]), but are too involved to describe here.

For ease of discussion, we will describe a wavelet collocation discretization of the momentum equation in what follows. The principles remain quite general however, and can be applied to the entire coupled reacting Navier-Stokes system. In one-dimensional problems and neglecting density variations, the momentum equation can be written as

$$\frac{\partial u}{\partial t} + u\frac{\partial u}{\partial x} + \rho^{-1}\frac{\partial p}{\partial x} = \rho^{-1}\frac{\partial \tau_{xx}}{\partial x}.$$

Our goal is to express this equation in terms of projected variables $P_J(\rho)$ and $P_J(u)$. Projecting the entire equation directly onto $\mathbf{V}_J$ leads to

$$\frac{\partial P_J(u)}{\partial t} + P_J\left(u\frac{\partial u}{\partial x}\right) + \rho^{-1}P_J\left(\frac{\partial p}{\partial x}\right) = \rho^{-1}P_J\left(\frac{\partial \tau_{xx}}{\partial x}\right). \tag{14.8}$$

The unsteady term does not provide any difficulties, since the time derivative commutes with the projector. Problems arise with the convective terms because: (a) we require an approximation for the derivative itself and (b) there is a non-linear product to incorporate.

As a model for the effect of non-linearities, consider a one dimensional velocity field $u(x)$ projected onto $\mathbf{V}_J$:

$$P_J(u) = \sum_{m\in Z} u_{J,m}\phi_{J,m}(x).$$

Consider further the non-linear term $P_J(u)P_J(u)$, which can be obtained as part of the convective term in Eq. 14.8. The explicit representation of this term is

$$P_J(u)P_J(u) = \sum_{m\in Z}\sum_{n\in Z} u_{J,m}u_{J,n}\phi_{J,m}(x)\phi_{J,n}(x) \notin \mathbf{V}_J. \tag{14.9}$$

In order to be consistent with the time derivative term, we must re-project Eq. 14.9 to obtain

$$\begin{aligned} P_J(P_J(u)P_J(u)) &= \sum_{\alpha\in Z}\sum_{m\in Z}\sum_{n\in Z} u_{J,m}u_{J,n} < \phi_{J,m}(\widetilde{x})\phi_{J,n}(\widetilde{x}), \widetilde{\phi}_{J,\alpha}(\widetilde{x}) > \phi_{J,\alpha}(x), \\ &= \sum_{\alpha\in Z} u_{J,\alpha}u_{J,\alpha}\phi_{J,\alpha}(x). \end{aligned} \tag{14.10}$$

More important is the effect of this non-linearity on spaces other than $\mathbf{V}_J$. For example, projecting Eq. 14.9 on to $\mathbf{W}_J$, we find

$$Q_J\left(P_J\left(u\right)P_J\left(u\right)\right)=\sum_{\alpha\in Z}\sum_{m\in Z}\sum_{n\in Z}u_{J,m}u_{J,n}<\phi_{J,m}\left(\widetilde{x}\right)\phi_{J,n}\left(\widetilde{x}\right),\widetilde{\psi}_{J,\alpha}\left(\widetilde{x}\right)>\psi_{J,\alpha}\left(x\right). \tag{14.11}$$

The normal consequence of the biorthogonality between $\mathbf{V}_J$ and $\mathbf{W}_J$ (i.e. the relation $Q_J\left(P_J\left(\cdot\right)\right)=0$) does not hold here, since we have two scaling functions. Hence

$$<\phi_{J,m}\left(\widetilde{x}\right)\phi_{J,n}\left(\widetilde{x}\right),\widetilde{\psi}_{J,\alpha}\left(\widetilde{x}\right)>\neq 0 \tag{14.12}$$

in general, even without explicitly evaluating Eq. 14.11, we see that the nonlinearity has extended the representation of $u\left(x\right)$ from $\mathbf{V}_J$ to $\mathbf{V}_{J+1}$ by populating $\mathbf{W}_J$. Similar arguments can be made for other wavelet spaces. This behaviour is the wavelet analogue of the spectral spreading caused by the convection driven convolution arising in Fourier based pseudo-spectral methods [5], and has been studied in some detail by Beylkin [3].

If $u\left(x\right)$ is sufficiently smooth, then the high resolution wavelet coefficients will be small in magnitude. Furthermore, their interactions (governed by the coupling matrix in Eq. 14.12) will also produce only small effects. It is natural then for a DNS exploiting wavelet thresholding to assume $\mathbf{V}_J$ is of a sufficiently high resolution that the additional components arising from the non-linearity are small with reference to the size of the non-trivial coefficients. We can then replace each of the terms in Eq. 14.8 by their projected counterparts i.e.

$$\begin{aligned}P_J\left(u\frac{\partial u}{\partial x}\right)&\simeq P_J\left(u\right)P_J\left(\frac{\partial u}{\partial x}\right)\\&\simeq P_J\left(u\right)P_J\left(\frac{\partial}{\partial x}P_J^{-1}P_J\left(u\right)\right)\end{aligned} \tag{14.13}$$

where the identity operator has been decomposed as $I=P_JP_J^{-1}$. As before, this expression will contain terms in both $\mathbf{V}_J$ and $\mathbf{W}_J$. To express the resulting term consistently, then, we write equation 14.13(b) as

$$P_J\left(P_J\left(u\right)\left(P_J\left(\frac{\partial}{\partial x}\right)P_J^{-1}P_J\left(u\right)\right)\right).$$

Using the interpolating properties of the basis, this becomes

$$P_J\left(P_J\left(u\right)\left(P_J\left(\frac{\partial}{\partial x}\right)P_J^{-1}P_J\left(u\right)\right)\right)=P_J\left(u\right)\left(P_J\left(\frac{\partial}{\partial x}\right)P_J^{-1}P_J\left(u\right)\right),$$

and we acknowledge that some information transmitted by this operation to $\mathbf{W}_J$ is lost. Similar expressions can be derived for the simpler, linear viscous and pressure terms.

14.3.1 The Wavelet Representation of the Derivative

The term

$$P_J \left(\frac{\partial}{\partial x} \right) P_J^{-1} \tag{14.14}$$

provides the representation of the differential operator on $\mathbf{V}_J$; Fig. 14.1 shows the $O\left(2^J\right)$ non-zero elements for this operator.

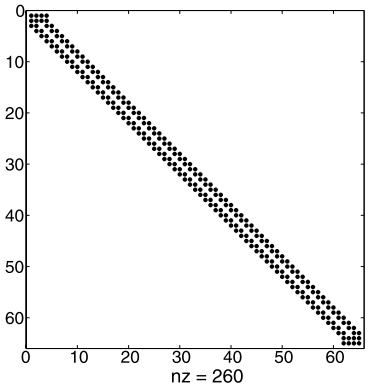

Fig. 14.1: Structure of $\mathbb{D}$ approximating $\frac{d}{dx}$ on $\mathbf{V}_J$. Reprinted from [26] wither permission from the Institution of Mechanical Engineers.

The derivative itself can be calculated as

$$\begin{aligned} \left(P_J \frac{\partial}{\partial x} P_J^{-1} \right) P_J(f)|_{x_{J,\alpha}} &= < \widetilde{\phi}_{J,\alpha}, \frac{\partial}{\partial x} \phi_{J,\beta} > P_J(f)|_{x_{J,\beta}}, \\ &= \mathbb{D}_{\alpha,\beta} \, P_J(f)|_{x_{J,\beta}}. \end{aligned}$$

In practice, the band diagonal structure of $\mathbb{D}_{\alpha,\beta}$ lends itself to a finite difference like implementation.

In order to take advantage of the sparsity in the wavelet representation of the flow field, the representations of both the operator and the flow field need to be expressed in terms of a multi-scale decomposition. Repeatedly applying Eq. 14.1 to Eq. 14.14 leads to the so-called standard decomposition of $\partial/\partial x$ [2, 4]:

$$\mathbb{D}^w = \left(P_j + \sum_{i=j}^{J} Q_i \right) \left(\frac{\partial}{\partial x} \right) \left(P_j + \sum_{i=j}^{J} Q_i \right)^{-1}.$$

This operator comprises a family of band diagonal sub-matrices which are ordered as in Fig. 14.2.

In terms of implementation, we have

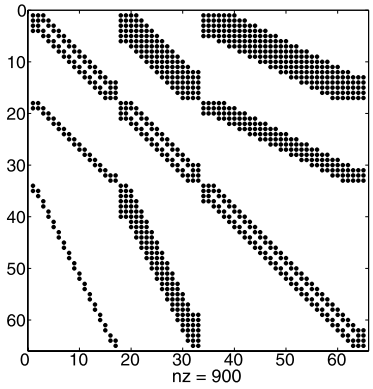

Fig. 14.2: Structure of $\mathbb{D}^w$ approximating $(P_{J-2} + \sum_{i=J-2}^{J-1} Q_i)\frac{d}{dx}(P_{J-2} + \sum_{i=J-2}^{J-1} Q_i)^{-1}$. Reprinted from [26] with permission from the Institution of Mechanical Engineers.

$$\left(P_j + \sum_{i=j}^{J} Q_i\right) \left.\frac{\partial f}{\partial x}\right|_{x_{J,\alpha}} \simeq \mathbb{D}^w_{\alpha,\beta} \left\{P_j + \sum_{i=j}^{J} Q_i\right\} (f)|_{x_{J,\beta}}.$$

$\mathbb{D}^w_{\alpha,\beta}$ is referred to as the standard decomposition of $\frac{\partial}{\partial x}$ [4] and typically comprises $O\left(2^J \log_2\left(2^J\right) = J \log 2^J\right)$ non-zero elements.

14.3.2 Higher Dimensional Discretizations

A natural generalisation to the one dimensional wavelets explored in this paper is achieved by deriving multidimensional analogues from first principles (i.e. [22]). For most practical purposes, however, multidimensional generalisations are derived via tensor products of one dimensional transforms, i.e. for a two dimensional discretisation, we define $\mathbf{V_J^{(2)}}$ using

$$\begin{aligned} \mathbf{V_J^{(2)}} &= \mathbf{V_{J-1}^{(2)}} \oplus \mathbf{W_{J-1}^{(2)}} \\ \mathbf{V_J^{(2)}} &= \mathbf{V_J^{(x)}} \otimes \mathbf{V_J^{(y)}}. \end{aligned} \tag{14.15}$$

By applying a two scale decomposition in each spatial direction to Eq. 14.15(b), we obtain

$$\mathbf{V_J^{(2)}} = \left(\mathbf{V_{J-1}^{(x)}} \oplus \mathbf{W_{J-1}^{(x)}}\right) \otimes \left(\mathbf{V_{J-1}^{(y)}} \oplus \mathbf{W_{J-1}^{(y)}}\right) \tag{14.16}$$

which when expanded, leads to the multidimensional wavelet space

$$\mathbf{W}_{\mathbf{J-1}}^{(\mathbf{2})} = \left(\mathbf{W}_{\mathbf{J-1}}^{(\mathbf{x})} \otimes \mathbf{V}_{\mathbf{J-1}}^{(\mathbf{y})}\right) \oplus \left(\mathbf{V}_{\mathbf{J-1}}^{(\mathbf{x})} \otimes \mathbf{V}_{\mathbf{J-1}}^{(\mathbf{y})}\right) \oplus \left(\mathbf{W}_{\mathbf{J-1}}^{(\mathbf{x})} \otimes \mathbf{W}_{\mathbf{J-1}}^{(\mathbf{y})}\right). \qquad (14.17)$$

Clearly, the wavelet space actually contains three contributions; the 'pure' wavelet space $\left(\mathbf{W}_{\mathbf{J-1}}^{(\mathbf{x})} \otimes \mathbf{W}_{\mathbf{J-1}}^{(\mathbf{y})}\right)$, and two 'cross' spaces: $\left(\mathbf{W}_{\mathbf{J-1}}^{(\mathbf{x})} \otimes \mathbf{V}_{\mathbf{J-1}}^{(\mathbf{y})}\right)$ and $\left(\mathbf{V}_{\mathbf{J-1}}^{(\mathbf{x})} \otimes \mathbf{W}_{\mathbf{J-1}}^{(\mathbf{y})}\right)$. Equation 14.16 may be further decomposed by splitting $\mathbf{V}_{\mathbf{J-1}}^{(\mathbf{x})}$ and $\mathbf{V}_{\mathbf{J-1}}^{(\mathbf{y})}$ into their respective scaling function and wavelet spaces of resolution $J-2$. The appearance of the two dimensional decomposition shares many similarities to the standard decomposition of $\frac{d}{dx}$. An example is provided in Figs. 14.3 and 14.4, which show an instantaneous realisation of the kinetic energy from a two dimensional 'turbulent' flow, and its associated multiresolution decomposition. In this case, $J = 8$, and there are 4 subspaces in each of the $x-$ and $y-$ directions. The lower left corner of Fig. 14.4 depicts an approximation to the original signal on $\mathbf{V}_{\mathbf{4}}^{(\mathbf{2})}$. Each of the subsequent subblocks growing out to the top right of the figure are associated with $\mathbf{W}_{\mathbf{i}}^{(\mathbf{x})} \otimes \mathbf{W}_{\mathbf{i}}^{(\mathbf{y})}$. The blocks above this diagonal correspond to spaces of the form $\mathbf{V}_{\mathbf{i}}^{(\mathbf{x})} \otimes \mathbf{W}_{\mathbf{m}}^{(\mathbf{y})}$ while those below correspond to $\mathbf{W}_{\mathbf{i}}^{(\mathbf{x})} \otimes \mathbf{V}_{\mathbf{m}}^{(\mathbf{y})}$. The particular point to note is the sparsity in the wavelet representation: away from the coarsest representations, the magnitudes of the wavelet coefficients are close to zero.

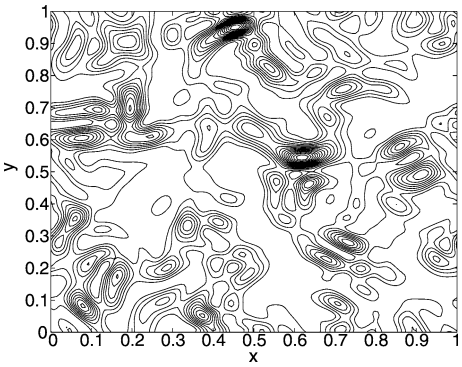

Fig. 14.3: Kinetic energy contours for 2D turbulence.

The practical application of wavelets to the Direct Numerical Simulation of reacting flows faces a number of difficulties. The non-linear terms associated with the chemical reaction rate (and, to a lesser extent, the convective term) effectively preclude the evolution of the simulation in the transform domain. Consequently, the transport equations must be time advanced in physical space. The wavelets are then used as part of a collocation strategy: (a) to inform the grid tracking algorithm of where points are required, and; (b) to calculate the derivatives on this reduced grid. The algorithmic difficulty is then one of correctly calculating the wavelet transform on a generally sparse grid.

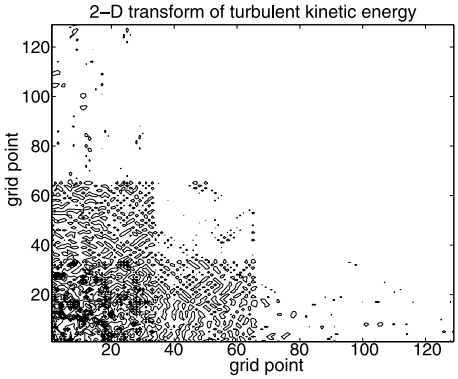

Fig. 14.4: 2D Wavelet transform of turbulent kinetic energy.

Most wavelet transforms are 'top-down' algorithms; the wavelet transform is obtained by the repeated application of quadrature mirror filters in a finite difference like algorithm. Each application of the filters to a high resolution signal produce two complementary low resolution signals (the scaling function coefficients and the wavelet coefficients). On a sparse grid, the so-called hanging node problem appears—grid points retained at the edge of a region of rapid change do not contain sufficient neighbour nodes to calculate their wavelet coefficients. The hanging node problem can be circumvented by a number of methods in 1-D (i.e. [31]), but the extension to 2-D is difficult. In the latter case, there is no unique way in which to order the wavelet coefficients, and multidimensional transforms lose their commutivity in the presence of a hard non linear threshold (i.e. a 2-D transform comprising $x-$ followed by $y-$ transforms will yield different coefficients to a 2-D transform comprising $y-$ followed by $x-$ transforms). Practical experience has shown that—particularly in low Mach number flows—the error induced by the hanging node problem manifests itself as a small perturbation in the dependent variables. These perturbations are picked up by the grid tracking algorithm as physical entities, and subsequently allowed to evolve. On the *new* hanging nodes thus formed, new perturbations are introduced and the grid grows again to accommodate these new features. The process repeats until the full grid is retained. Circumventing this problem forms part of ongoing research efforts.

14.4 An Application of Wavelets to Reacting Flows

14.4.1 Governing Equations

The equations governing a chemically reacting flow in one dimension are given by

$$\frac{\partial \rho}{\partial t} + \frac{\partial}{\partial x}(\rho u) = 0$$
$$\frac{\partial \rho u}{\partial t} + \frac{\partial}{\partial x}(\rho uu + p) = \frac{\partial}{\partial x}(\tau_{xx})$$
$$\frac{\partial \rho E}{\partial t} + \frac{\partial}{\partial x}(u(\rho E + p)) = -\frac{\partial q}{\partial x} + \frac{\partial}{\partial x}(u\tau_{xx})$$
$$\rho \frac{\partial \rho Y_l}{\partial t} + \frac{\partial}{\partial x}(\rho u Y_l) = \omega_l + \frac{\partial}{\partial x}\left(\rho D \frac{\partial Y_l}{\partial x}\right) \qquad l = 1, 2, \ldots, N_s - 1. \quad (14.18)$$

where $N_s > 1$ is the number of species, τ_{xx} is the viscous stress and the heat flux vector q is defined as

$$q = -\lambda \frac{\partial T}{\partial x} - \sum_{l=1}^{N_s} h_l \rho D \frac{\partial Y_l}{\partial x}. \quad (14.19)$$

For simplicity, the chemical reaction is assumed to comprise the single step

$$\text{Reactants} \rightarrow \text{Products}$$

in which case, $N_s = 2$ and the thermochemical state of the gas is characterized by a *progress variable*. The progress variable is interpreted as a normalized product mass fraction, and takes a value of 0 in the reactants and 1 in the products. $c = Y_1$ here and $Y_2 = 1 - Y_1$. The reaction rate controlling the production of c is given by [32]

$$\omega_1 = \rho B^* (1 - c) \exp\left(\frac{-\beta\left(1 - \widehat{T}\right)}{1 - \alpha\left(1 - \widehat{T}\right)}\right),$$

with $\omega_2 = -\omega_1$. B^* is the pre-exponential factor (taken to be $285.1 \times 10^{-3} s^{-1}$ here), $\beta (= 6)$ is the Zeldovich number and $\widehat{T}$ is the reduced temperature;

$$\widehat{T} = \frac{T - T_0}{T_{ad} - T_0}.$$

T_0 and T_{ad} are the unburned reactant and adiabatic product temperature, respectively. α is related to the heat release of the fuel, and is set here to 0.8. This corresponds to an adiabatic flame temperature of 1500 K for an inlet temperature of 300 K. The reaction rate has been adjusted to give a laminar flame speed of ~ 30 cm/s, a value typical of many hydrocarbon-air flames. The inlet velocity is set equal to the laminar flame speed, so that a stationary flame profile is obtained. This specification gives a simulation Mach number of $O\left(10^{-3}\right)$ based on the laminar flame speed. The thermal conductivity is a modified form of the equation proposed by Echekki et al. [13]:

$$\lambda = \lambda_0 c_p \left(\frac{T}{T_0}\right),$$

where $\lambda_0 = 2.58 \times 10^{-5}$ kg/(ms). The temperature dependence of the conductivity has been chosen such that the resulting temperature and species profiles can be de-

rived analytically using asymptotic methods [32]. The viscosity and mass diffusion are calculated via the joint assumptions of constant Prandtl number (= 0.75) and constant unit Lewis number. The other thermodynamic quantities are assumed to be constant and are set equal to the values given for air. The stagnation internal energy is obtained using

$$E = \sum_{l=1}^{N_s} e_l Y_l + \frac{u^2}{2},$$

where e_l is the species internal energy, comprising the internal energy of formation e_l^0, and a sensible component:

$$e_l = e_l^0 + \int_{T_0}^{T} c_v\left(T'\right) dT'.$$

The specific heats and the molecular weights of the components are assumed to be constant, with $c_p = 1005$ J/(kg K), $\gamma = 1.4$ and $W = 28.96$ kg/kmol. The pressure is calculated from the thermal equation of state

$$p = \rho \mathscr{R}^0 T \sum_{l=1}^{N_s} \frac{Y_l}{W_l}, \tag{14.20}$$

where $\mathscr{R}^0$ (=8314.5 J/(kmol K)) is the universal gas constant.

The governing equations retain full compressibility, and hence acoustic waves will need to be accurately captured by the wavelets. This has been done deliberately, since the accurate resolution of the pressure profile provides a stringent challenge for the discretization.

14.5 Results

Figures 14.5(a)-(d) show a benchmark solution for a 1-D laminar flame. The solution has been calculated using $N = 4$ interpolating wavelets and initially with wavelet thresholding switched off (i.e. using a full grid). The discretization comprises initially $2^8 + 1$ (i.e. $\mathbf{V}_J = \mathbf{V}_8$) grid points; the extra grid point comes from end effects introduced via discretizing an interval.

Figure 14.6 shows a comparison between the benchmark solution and an analytic profile obtained by high activation energy asymptotics [32]; the agreement between the two is excellent, and thereby establishes the credibility of wavelets as a means of DNS.

Figure 14.7 shows the reaction rate profile and the retained grid points, the latter being obtained by thresholding the wavelet series based on the magnitudes of the respective dependent (conservative) variables. The automatic clustering of the grid points in the region of the flame are the principal driver for the development of wavelet methods.

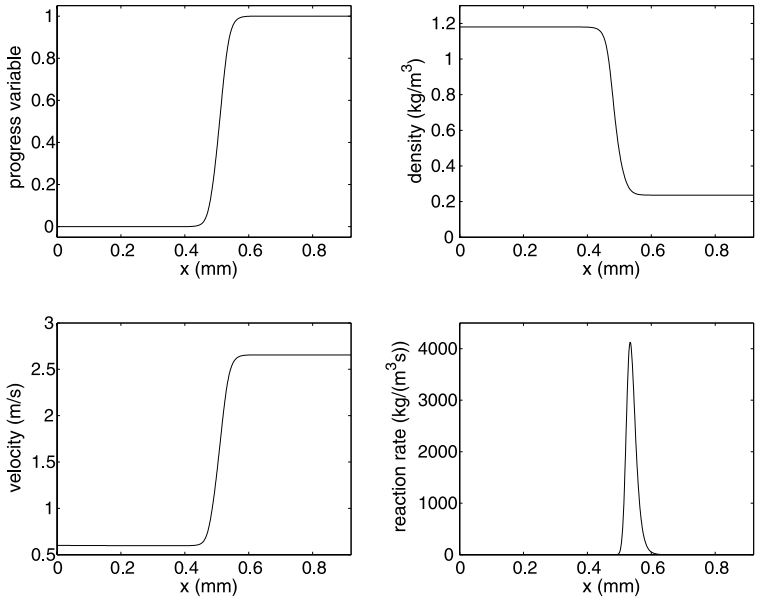

Fig. 14.5: Benchmark laminar flame profile.

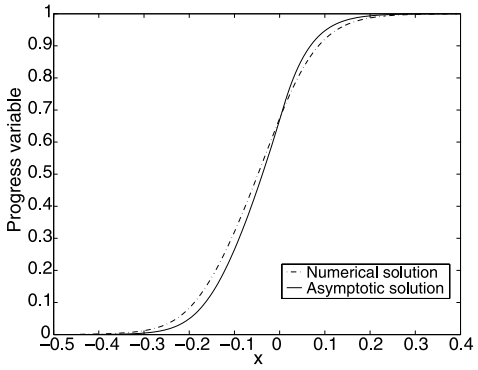

Fig. 14.6: Progress variable profile obtained analytically and numerically with $\varepsilon = 0$. Reprinted from [26] wither permission from the Institution of Mechanical Engineers.

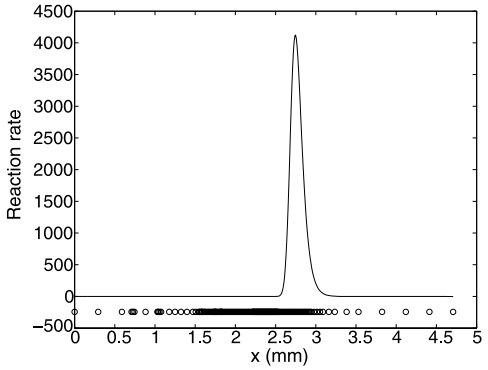

Fig. 14.7: Reaction rate. ○ denotes location of retained grid points.

The effects of increasing threshold ε on the temperature profile have been found to be essentially invisible. Of more interest is the effect of thresholding on the resolution of the pressure profile. It is well known that low Mach number systems exhibit stiffness (i.e. see Klein [18]); this stiffness manifests itself here as a pressure profile that is extremely sensitive to numerical noise. Figures 14.8, 14.9 and 14.10 show the pressure profile obtained with increasing thresholds. The dynamic pressure change is itself very small, and so consequently is quite sensitive to any perturbation.

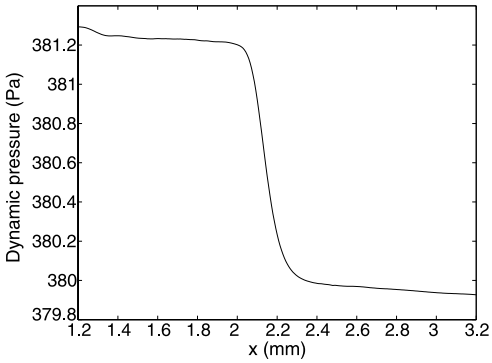

Fig. 14.8: Dynamic pressure profile for thresholded solution, with $\varepsilon = 10^{-6}$. Reprinted from [26] wither permission from the Institution of Mechanical Engineers.

An estimate for the effect of wavelet thresholding on pressure can be established for low Mach number systems by examining the thermodynamic relationship between the conserved variables and the pressure. Using standard thermodynamic relations, the change in pressure for a mixture of N_s ideal gases can be related to changes in the conserved variables by

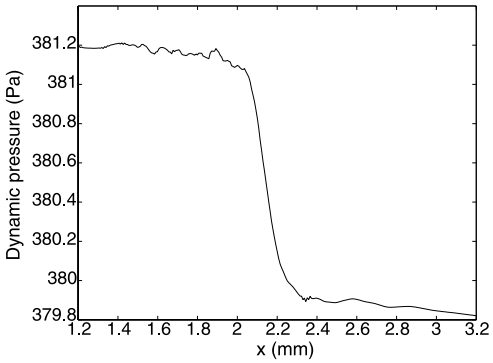

Fig. 14.9: Dynamic pressure profile for thresholded solution, with $\varepsilon = 10^{-5}$. Reprinted from [26] wither permission from the Institution of Mechanical Engineers.

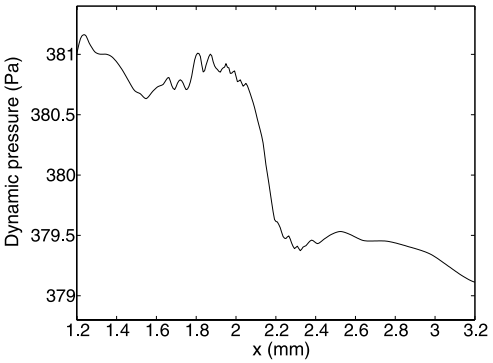

Fig. 14.10: Dynamic pressure profile for thresholded solution, with $\varepsilon = 10^{-4}$. Reprinted from [26] wither permission from the Institution of Mechanical Engineers.

$$dp = (\gamma-1)\left[d(\rho E) - ud(\rho u) + \frac{1}{2}u^2 d\rho\right] - \sum_{\alpha=1}^{N_s}\left((\gamma-1)e_\alpha - R_\alpha T\right)d(\rho Y_\alpha). \tag{14.21}$$

A better understanding of the relative effects can be obtained by non-dimensionalising Eq. 14.21 to obtain

$$dp = (\gamma-1)\left[d(\rho E) - (\gamma-1)M^2\left(ud(\rho u) - \frac{1}{2}u^2 d\rho\right)\right] - \sum_{\alpha=1}^{N_s}\left(\widetilde{e}_\alpha - \frac{R_\alpha T}{(\gamma-1)}\right)d(\rho Y_\alpha), \tag{14.22}$$

where the pressure has been non-dimensionalized with respect to $\gamma\rho^0 RT_0$; the remaining quantities have been non-dimensionalized with respect to u_0, $(c_p)_0$ and T_0. Consider a discretization which decomposes $\mathbf{V}_J$ onto $\mathbf{V}_{J-1}$ and $\mathbf{W}_{J-1}$ for clarity. At some point during the integration, the solution is transformed onto $\mathbf{V}_{J-1}$ and $\mathbf{W}_{J-1}$, and then a threshold is applied. The resultant reduced series is then used to reconstruct the dependent variables. This procedure is a model for an adaptive solution algorithm where in this case, the missing coefficients are replaced with a zero in the transform domain.

By construction in this simple example, errors of $O(\varepsilon)$ are incurred in the energy, the momentum, the density and the species mass fraction profiles. Using equation 14.22, we write

$$\Delta p = (\gamma-1)\left[\Delta(\rho E) - (\gamma-1)M^2\left(u\Delta(\rho u) - \frac{1}{2}u^2\Delta\rho\right)\right] - \sum_{\alpha=1}^{N_s}\left(\widetilde{e}_\alpha - \frac{R_\alpha T}{(\gamma-1)}\right)\Delta(\rho Y_\alpha) \tag{14.23}$$

where the Δ symbol is used to denote the departure from the benchmark solution as a result of thresholding:

$$\begin{aligned}\Delta p &= p - p^\varepsilon\\ \Delta(\rho E) &= (\rho E) - (\rho E)^\varepsilon\\ \Delta(\rho) &= \rho - \rho^\varepsilon\\ \Delta(\rho Y_\alpha) &= (\rho Y_\alpha) - (\rho Y_\alpha)^\varepsilon.\end{aligned}$$

It is clear that both the momentum and density driven effects will be very small $\left(O\left(M^2\right) \sim 10^{-6}\varepsilon\right)$ in comparison to those effects induced by errors in the energy and species mass fraction, which are both of $O(\varepsilon)$. Consequently, in any adaptive numerical strategy it is important to use at least ρE and (ρY_α) as the key variables upon which the unstructured grid is built. If the previous analysis is extended to a multiresolution decomposition, essentially the same argument holds, but with the magnitudes of the errors $\Delta(\cdot)$ increased by a factor of approximately $O(J)$ where J refers to the index of the original discretisation.

Interestingly, a similar problem is observed if asynchronous time evolution methods are employed (i.e. the schemes proposed by Bacry et al. [1]). It appears that the coupling engendered by the pressure (through the energy equation) links phenomena across many different scales, all of which interact with equal importance.

14.6 Conclusions

Wavelets have enjoyed considerable popularity in recent years. Their utility stems from the scale and position dependent decompositions they provide, which in turn

furnishes flow descriptions with a level of fidelity beyond that offered by Fourier transforms (which are spatially delocalized). Considerable effort has gone into the exploitation of wavelets for reacting flow simulation. They provide a natural framework to produce adaptive computations, although some technical challenges remain regarding inertial and chemistry driven non-linearity (this problem however is prevalent to some extent with any numerical scheme). We have discussed in some detail one possible line of attack for reacting flows involving interpolating wavelets. Others are available (i.e. the vaguelettes of Schneider et al. [15–17]). We have chosen to describe the interpolating wavelet approach because of the closeness of the discretisation to existing engineering calculation methods (i.e. it needs no initial projection quadrature, nor operator modified vaguelettes, etc.)

In addition, the discussions presented here regarding non-linearities and differential operators are not restricted to the arena of DNS. We have seen how new wavelet spaces may be populated during a nonlinear interaction. Furthermore, there is a clear path from this emergent population to all other scales through the medium of the differential operator. We may interpret mappings of the form $\mathbf{W}_i \rightarrow \mathbf{W}_k \; k > i$ within the operator as being akin to an inertial cascade processes, while the converse represents backscatter. Hence, wavelets provide a scale and position dependent method of identifying and predicting the emergent phenomena in a turbulent flow and of estimating how that phenomena affects the resolved field. A modelling strategy may exploit this by estimating the magnitudes of the wavelet coefficients emerging from the non-linearity, and using the (known) values of the operator to estimate the effects on the resolved scales. Such studies have been undertaken by a number of workers (i.e. [10]), but further work is yet required.

References

1. Bacry, E., Mallat, S.G., Papanicolaou, G.: A wavelet based space-time adaptive numerical method for partial differential equations. Math. Modelling Num. Anal. **26**, 793–834 (1992)
2. Beylkin, G.: On the representation of operators in bases of compactly supported wavelets. SIAM J. Num. Anal. **6**, 1716–1740 (1992)
3. Beylkin, G.: On the fast algorithm for multiplication of functions in the wavelet bases. International Conference on Wavelets and Applications (1992)
4. Beylkin, G., Coifman, R., Rokhlin, V.: Fast wavelet transforms and numerical algorithms I. Commun. Pure Appl. Math. **44**, 141–183 (1991)
5. Canuto, C., Hussaini, M.Y., Quarteroni, A., Zang, T.: Spectral Methods in Fluid Dynamics, Springer-Verlag (1988)
6. Cohen, A., Daubechies, I., Feauveau, J.C.: Biorthogonal bases of compactly supported wavelets. Commun. Pure Appl. Math. **45**, 485–460 (1992)
7. Cohen, A., Daubechies, I., Vial, P.: Wavelets on the interval and fast wavelet transforms. Appl. Comp. Harmonic Analysis **1**, 54–81 (1993)
8. Daubechies, I.: Ten lectures on wavelets, SIAM, Philadelphia (1992)
9. Day, M., Bell, J., Bremer, P.-T., Pascucci, V., Beckner, V., Lijewski, M.: Turbulence effects on cellular burning structures in lean premixed hydrogen flames. Combust. Flame **156**, 1035–1045 (2009)
10. de la Llave Plata, M., Cant, R.S.: On the application of wavelets to LES subgrid modelling. Quality and Reliability of Large Eddy Simulations (QLES07) (2007)

11. Deslauriers, G., Dubuc, S.: Symmetric iterative interpolation processes. Constr. Approx. **5**, 49–68 (1989)
12. Donoho, D.L.: Interpolating wavelet transforms. Presented at The NATO Advanced Study Institute conference on Wavelets and Applications, Il Ciocco, Italy (1992)
13. Echekki, T., Chen, J.H.: Unsteady strain rate and curvature effects in turbulent premixed methane-air flames. Combust. Flame **106**, 184–202 (1996)
14. Fernández, G., Periaswamy, S., Sweldens, W.: LIFTPACK: A software package for wavelet transforms using lifting. Wavelet Applications in Signal and Image Processing IV, Proc. SPIE, 396–408 (1996)
15. Fröhlich, J., Schneider, K.: An adaptive wavelet-vaguelette algorithm for the solution of PDEs. J. Comput. Phys. **130**, 174–190 (1997)
16. Fröhlich, J., Schneider, K.: Numerical simulation of decaying turbulence in an adapted wavelet basis. Appl. Comput. Harm. Anal. **2**, 393–397 (1995)
17. Fröhlich, J., Schneider, K.: A fast algorithm for lacunary wavelet bases related to the solution of PDEs. C. R. Math. Rep. Acad. Sci. Canada **16**, 83–86 (1996)
18. Klein, R.: Semi-implicit extension of a Godunov-type scheme based on low Mach number asymptotics I: One dimensional flow. J. Comput. Phys. **121**, 213–237 (1995)
19. Jameson, L.: On the Daubechies based wavelet differentiation matrix. NASA ICASE Report 93-95 (1993)
20. Jameson, L.: On the differentiation matrix for Daubechies-based wavelets on an interval. SIAM J. Sci. Comput. **17**, 498–516 (1996)
21. Mallat, S.G.: A theory for multiresolution signal decomposition: The Wavelet representation. IEEE Trans. Pattern Anal. Machine Intell. **11**, 674–692 (1989)
22. Meyer, Y.: Wavelets and Operators, Cambridge University Press (1992)
23. Newland, D.E.: Harmonic wavelet analysis. Proc. Roy. Soc. Lond. A **443**, 203–25 (1993)
24. Press, W.H., Teukolsky, S.A., Vetterling, W.T., Flannery, B.P.: Numerical Recipes in FORTRAN, Cambridge University Press (1992)
25. Prosser, R.: Numerical methods for the computation of cmbustion. Ph.D. Thesis, Cambridge University (1997)
26. Prosser, R.: An adaptive algorithm for compressible reacting flows using interpolating wavelets. Proc. Instn. Mech. Engrs. Part C **221**, 1397–1410 (2007)
27. Schröder, P., Sweldens, W.: Building your own wavelets at home. Lecture Notes in Earth Sciences Vol. 90, Springer (2000)
28. Sharpe, G.J., Falle, S.A.E.G.: Nonlinear cellular instabilities of planar premixed flames: numerical simulations of the reactive Navier-Stokes equations. Combust. Theor. Model. **10**, 483–514 (2006)
29. Sweldens, W.: The Lifting scheme: A custom design construction of biorthogonal wavelets. Appl. Comput. Harm. Anal. **3**, 186–200 (1996)
30. Sweldens, W.: The Lifting scheme: A construction of second generation wavelets. SIAM J. Math. Anal. **29**, 511–546 (1997)
31. Vasilyev, O.V., Kevlahan, N.K.R.: An adaptive multilevel wavelet collocation method for elliptic problems. J. Comput. Phys. **206**, 412–431 (2005)
32. Williams, F.A.: Combustion Theory - Second Edition, Addison Wesley (1985)